Article

Not peer-reviewed version

Long Short-Term Memory Recurrent Network Architectures for Electromagnetic Field Reconstruction Based on Underground Observations

Yixing Tian , Chengliang Xie * , Yun Wang

Posted Date: 21 May 2024

doi: 10.20944/preprints202405.1347.v1

Keywords: underground laboratory; electromagnetic field; neural network; noise suppression; LSTM

Article

Long Short-Term Memory Recurrent Network Architectures for Electromagnetic Field Reconstruction Based on Underground Observations

Yixing Tian [1,2], Chengliang Xie [1,2,*] and Yun Wang [1,2]

[1] Key Laboratory of Intraplate Volcanoes and Earthquakes (China University of Geosciences, Beijing), Ministry of Education, Beijing 100083, China; tianyixing2000@163.com (Y.T.); wangyun@mail.gyig.ac.cn (Y.W.)

[2] School of Geophysics and Information Technology, China University of Geosciences, Beijing 100083, China

* Correspondence: clx@cugb.edu.cn; Tel.: +8615201018722

Abstract: Deep underground laboratories offer advantages for conducting high-precision observations of weak geophysical signals, benefitting from a low background noise level. It is both valuable and feasible to enhance strong, noisy ground electromagnetic (EM) field data using synchronously recorded underground EM signals, which typically exhibit a high signal-to-noise ratio. In this study, we propose an EM field reconstruction method employing a Long Short-Term Memory (LSTM) recurrent neural network with referenced deep underground EM observations. Initially, a deep learning model was developed to capture the time-varying features of underground multi-component EM fields using the LSTM recurrent neural network. Subsequently, this model was applied to process synchronously observed strong, noisy data from other conventional observation systems, such as those at surface, to achieve noise suppression through signal reconstructions. Both theoretical analysis and practical observational data suggest that the proposed method effectively suppresses noise and reconstructs clean EM signals. This method is efficient and time-saving, representing an effective approach to fully utilizing the advantages of deep underground observation data. Furthermore, this method could be extended to the processing and analysis of other geophysical data.

Keywords: underground laboratory; electromagnetic field; neural network; noise suppression; LSTM

1. Introduction

Deep underground spaces are characterized by low background noise, low cosmic ray intensity, and limited electromagnetic radiation. These features make underground laboratories crucial locations for research across microphysics, astrophysics, cosmology, and geoscience [1]. Over the past decades, numerous international underground laboratories have been constructed and continuously developed, including SNO in Canada [2], Kamioka in Japan [3], Modane and LSBB in France [4,5], Boulby in the UK [6], Baksan in Russia [7,8], and SarGrav in Italy [9,10], among others. These underground laboratories have volumes ranging from a few hundred to thousands of cubic meters, with vertical rock cover thicknesses ranging from a few hundred meters to over 2,000 meters. The thick cover layer offers an ideal low-background environment for experimental research across various disciplines [11]. Some underground laboratories have conducted multi-geophysical field observations, such as LSBB in France, where superconducting magnetometers were employed to observe magnetic field signals, showcasing the inherent advantages of deep underground environments in capturing weak electromagnetic signals [12]. Since 2020, collaborative observations of multi-geophysical fields have been conducted in the Huainan underground laboratory (HNLab) in China. These observations demonstrate that underground environments have advantage and

 doi:10.20944/preprints202405.1347.v1

potential for sustained, stable observations of geophysical fields [13–19]. However, geophysical fields observations in HNLab are still in the early stages [16], and numerous challenges remain, including experimental method design, underground lab infrastructure renovation, and instrument research and development. Furthermore, it is essential to fully utilize observational data from 'ultra-silent' and 'ultra-clean' environments to explore their potential in denoising traditional surface observation signals.

Magnetotelluric (MT) is a geophysical method used to observe natural time-varying electromagnetic fields for probing subsurface geo-electrical structures. MT has been widely employed to investigate crust and mantle structures, subsurface deformations, and deep processes. However, the weak natural EM field signals are susceptible to contamination by various anthropogenic noises, significantly limiting the practical effectiveness of MT. To obtain stable and high signal-to-noise ratio EM signals, improving MT technology has become a key focus [20,21]. A typical MT data processing algorithm aims to optimize superimposed partial transfer functions or power spectral density matrices across all frequency domain windows. This process involves identifying, eliminating, and weighting outliers in the time and/or frequency domain. However, the measured data often deviate from an ideal Gaussian distribution, rendering traditional least squares methods less effective. Manually labeling of time slices or partial power spectral density matrices is a direct but time-consuming and inefficient method for enhancing superposition. Robust estimations based on various regression algorithms can mitigate the impact of outliers induced by random impulse noise [22–25]. However, robust results are challenging to achieve when noise persists throughout the entire observation period. Another effective approach is the remote reference method, which suppresses uncorrelated noise between local and remote stations by utilizing an additional "clean" remote station [26–28]. This method is commonly applied using magnetic channels, leveraging strong correlations among regional signals. In cases where array datasets are available, frequency domain principal component analysis is a reliable processing approach using Fourier coefficient vectors from multi-channels across multi-stations [29–32]. This method reduces the dimensionality of high-dimensional datasets to lower dimensions, enhancing processing efficiency. However, the multiple-channel algorithm requires specific data quality and quantity criteria to achieve optimal results. The mentioned methods often involve a short-time Fourier transform. Additionally, MT data processing utilizes other transforms and digital signal processing algorithms, such as the wavelet transform [33], the Hilbert–Huang Transform [34], Empirical Mode Decomposition [35], compressive sensing technology [36], Wiener filtering [37], independent component analysis [38], blind source separation method [32], and among others. These methods demonstrate effectiveness in improving processing outcomes when dealing with typically distributed noise, provided that specific parameters are appropriately defined. However, they can be challenging to apply effectively in scenarios involving complex and strong noise.

Processing initial time series data, including noise recognition, removal, and signal reconstruction, represents direct and effective approaches to enhance the signal-to-noise ratio. In recent years, owning to continuous advancements in computer technology, deep learning algorithms have provided unique advantages in signal analysis and data processing, becoming crucial tools in geoscience [39]. Theses algorithms have been successfully applied to optimize and process EM field data. Manoj and Nagarajan [40] utilized artificial neural networks to identify and remove noise segments from EM data. This method requires manual identification and labeling of features, such as data quality and signal correlation, in the training dataset. Li et al. [41] employed a convolutional neural network (CNN) to construct a nonlinear mapping model between noisy data and noise contours. Li et al. [42] proposed a denoising algorithm combining CNNs and long-short term memory (LSTM) recurrent neural networks. Initially, signal-to-noise separation is conducted using CNNs, and then the LSTM model is trained with denoised data from the CNNs to predict clean data from noisy signals. However, significant misfits may occur when continuous noise exists in time series or when the length of noisy data is too long. Han et al. [43] developed a noise suppression method using LSTM networks, and the reconstructed data were employed in 2D inversion modeling, effectively suppressing strong noise with typical morphological features. However, lower accuracy can result

 doi:10.20944/preprints202405.1347.v1

when noisy and clean datasets exhibit similar morphological features. Most typical deep learning-based noise suppression methods are designed for single-channel data. Zhang et al. [44] proposed a multi-channel approach using CNNs and applied the method in audio magnetotelluric data processing, although longer period data remain ambiguous. The efficacy of supervised learning-based methods depends on available training datasets that encompass the principal signal and noise morphological features. Additionally, unsupervised data-driven deep learning techniques based on sparse coding algorithms are employed in noise identification, separation, and suppression of EM data, such as K-SVD dictionary learning [45–47], improved shift-invariant sparse coding [48], and adaptive sparse representation [49], among others. However, appropriately defining specified coefficients is essential for these methods, often requiring multiple experiments to achieve optimal results. Furthermore, two key dataset conditions are necessary to ensure efficacy: a sufficient high signal-to-noise ratio and strong regularity characteristics [45].

Robust training models play crucial roles in ensuring successful time series denoising outcomes. Generally, supervised learning algorithms use labeled training datasets to generalize training models [50], and having a rich and representative training dataset is crucial to ensure good generalization ability of the model in practical applications. Traditionally, typical EM noises such as charge and discharge triangle waves, square waves, peak noise, and step noise are superimposed on clean measured and/or theoretical data to construct the training datasets [41–44]. However, constructing sufficient sample libraries that encompass various complex noise features of practical data can be challenging. Although data-driven algorithms such as dictionary learning based on sparse coding [45–49] can be used to obtain atoms that match the target signal directly from the observed data, the applicability of such methods when faced with persistent and strong noise interference still requires further investigation.

In this study, we propose a signal reconstruction method based on LSTM neural networks using underground EM observation data. The method eliminates the need to pre-construct a database comprising a substantial number of synthesized signals and noises. Instead, it utilizes clean and stable multi-channel data from underground observations as the model training set in a data-driven manner. This approach allows the method to fully learn regional EM field variations and characteristics. Subsequently, noise suppression or **"**cleaning**"** is achieved through the process of signal reconstruction using noisy segments from synchronously observed ground data.

2. Theory and Method

2.1. Recurrent Neural Network

Recurrent Neural Networks (RNNs) excel in processing time series by capturing correlations between data points that are close in the sequence [51]. Unlike traditional neural networks, RNNs maintain a 'state vector' in their hidden units that implicitly retains information about the history of all past elements in the sequence [52]. This capability allows RNNs to overcome challenges related to backward and forward dependencies encountered by traditional neural networks.

Figure 1 illustrates a schematic diagram depicting the process of unfolding an RNN into a complete network. At time moment t, the input is denoted by $\mathbf{X}_t$, the output of the hidden layer neuron is denoted by $\mathbf{S}_t$, and the output is denoted by Ot. The corresponding weight matrices are represented by **U**, **V**, and **W**. The calculation of $\mathbf{S}_t$ involves the input $\mathbf{X}_t$ at the current time and the output ($\mathbf{S}_{t-1}$) of the previous hidden layer neuron (Equation (1)),

$$\mathbf{S}_t = f(\mathbf{U}\mathbf{X}_t + \boldsymbol{W}\boldsymbol{S}_{t-1} + \boldsymbol{b}_s), \tag{1}$$

The activation function for the hidden layer is typically either tanh or ReLU. The weight matrices are represented by **U** and **W**, and the bias vector is denoted by $\mathbf{b}_s$.

Preprints.org (www.preprints.org) | NOT PEER-REVIEWED | Posted: 21 May 2024 doi:10.20944/preprints202405.1347.v1

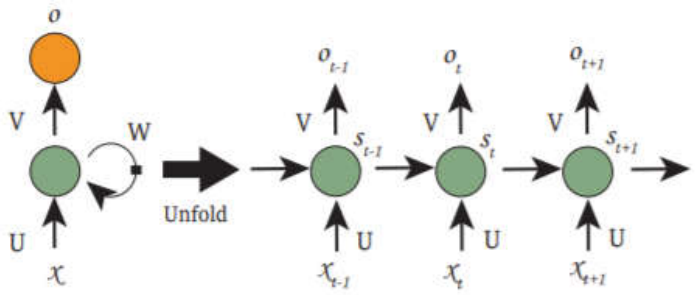

Figure 1. Recurrent neural networks (RNNs) and unfolding in time.

Equation (2) illustrates the relationship between the neuron input $\mathbf{S}_t$ and the output $\mathbf{O}_t$,

$$\boldsymbol{O}_t = g(\boldsymbol{V}\boldsymbol{S}_t + \boldsymbol{b}_o), \tag{2}$$

The activation function of output layer, typically SoftMax, is denoted by g. The weight matrix is denoted by V, and the bias vector is denoted by b_o.

Recurrent neural networks exhibit a memory effect when processing time series data. This structure enables RNNs to store, remember, and process past complex signals over extended time periods [53].

2.2. Long Short-Term Memory Neural Network

RNN can be considered as a deep feed-forward neural network where all layers share the same weights. However, during the model training phase, issues such as exploding gradients or vanishing gradients can arise, making it challenging to learn long-term dependencies in the data [53,54]. LSTM Networks are a variant of RNNs designed to overcome the limitations of traditional RNNs in capturing long-term dependencies within sequences and addressing challenges such as exploding gradient and vanishing gradients [55,56]. LSTM has the capability to address a wide range of tasks, such as text recognition, natural language processing, image and video description, sentiment analysis, and computer vision. Additionally, it has demonstrated significant efficacy in processing time series data [57].

As depicted in Figure 2, LSTM incorporates cell states to retain long-term information. The cell state functions akin to a conveyor belt, running directly through the entire sequence with minimal linear interactions [58]. Controlling this cell state is pivotal to LSTM, and the concept of gates is introduced to manage this process. These gates regulate information flow within hidden neurons, enabling the preservation of extracted features from previous timesteps [59].

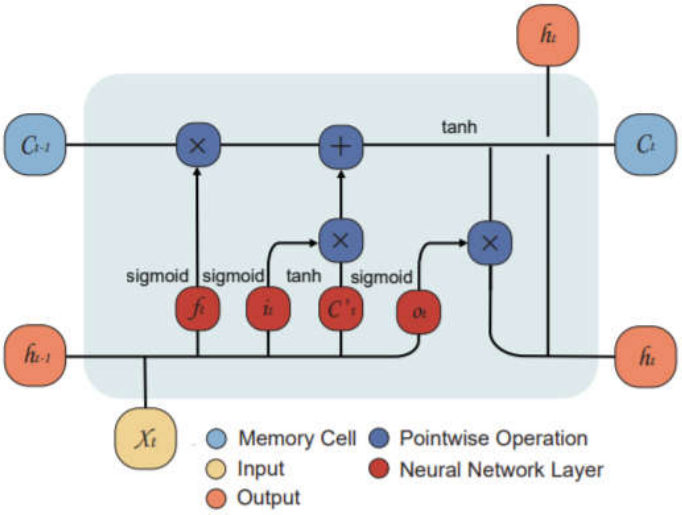

Figure 2. Structure of Long Short-Term Memory unit.

 doi:10.20944/preprints202405.1347.v1

The forget gate ($\mathbf{f}_t$) determines the extent to which the previous cell state ($\mathbf{C}_{t-1}$) at the previous time step is retained in the current cell state ($\mathbf{C}_t$) at the current time step,

$$\mathbf{f}_t = \sigma\left(\boldsymbol{x}_t \mathbf{W}_{xf} + \mathbf{h}_{t-1}\mathbf{W}_{hf} + \mathbf{b}_f\right), \tag{3}$$

The input gate ($\mathbf{i}_t$) determines the extent to which the current input ($\mathbf{x}_t$) at the current time step is retained in the current cell state ($\mathbf{C}_t$),

$$\mathbf{i}_t = \sigma(\mathbf{x}_t \mathbf{W}_{xi} + \mathbf{h}_{t-1}\mathbf{W}_{hi} + \mathbf{b}_i), \tag{4}$$

The candidate cell state ($\mathbf{C'}_t$) describing the current input ($\mathbf{x}_t$) is expressed as,

$$\mathbf{C'}_t = \tanh(\mathbf{x}_t \mathbf{W}_{xc} + \mathbf{h}_{t-1}\mathbf{W}_{hc} + \mathbf{b}_c), \tag{5}$$

The current cell state ($\mathbf{C}_t$) is then determined as,

$$\mathbf{C}_t = \mathbf{f}_t \odot \mathbf{C}_{t-1} + \mathbf{i}_t \odot \mathbf{C'}_t, \tag{6}$$

The output gate ($\mathbf{o}_t$) regulates the transfer of the cell state ($\mathbf{C}_t$) to the current output ($\mathbf{h}_t$),

$$\mathbf{o}_t = \sigma(\mathbf{x}_t \mathbf{W}_{xo} + \mathbf{h}_{t-1}\mathbf{W}_{ho} + \mathbf{b}_o), \tag{7}$$

Ultimately, the output of the LSTM (ht) is determined by combining the output gate (o_t) with the cell state (C_t),

$$\mathbf{h}_t = \mathbf{o}_t \odot \tanh(\mathbf{C}_t), \tag{8}$$

In the above equations, $\mathbf{W}$ represents the weight matrix, $\mathbf{b}$ represents the bias vector, $\mathbf{h}_{t-1}$ and $\mathbf{h}_t$ denote the hidden states of the previous and current time steps, respectively. The function σ represents the sigmoid function, and $\odot$ denotes the Hadamard product.

In summary, the LSTM recurrent neural network introduces the mechanism of cell states and 'gates' and offers advantages in capturing long-term dependencies. Challenges such as vanishing gradient or exploding gradient in traditional RNNs are overcome in the LSTM, enabling the neural network to preserve information over extended durations [60]. The LSTM network features a self-connection at the next time step with a weight. This connection allows the network to copy its own real-valued state and accumulates external signal. Moreover, this self-connection is gated by another unit, which learns to determine when to clear the content of the memory [52]. The LSTM model is sensitive to time and can effectively learn features present in time series data. This capability proves advantageous in tasks like time series prediction and signal processing [61], making it suitable for operations such as EM signals reconstruction and noise suppression.

2.3. Reconstruction of Electromagnetic Data

The EM signal reconstruction method based on underground data and LSTM recurrent neural network involves two main phases: (1) Model training: Utilizing underground EM data as the training dataset, the LSTM recurrent neural network is trained. (2) Signal reconstruction: The noisy sections of synchronously observed ground EM data are reconstructed to enhance data quality. Figure 3 depicts the flowchart of this data reconstruction method, illustrating the underground environment and station deployment with EM observation experiments conducted in HNLab. The LSTM network model consists of an input layer, one or multiple hidden layers, and an output layer. The input layer receives multi-channel EM time series, which is then processed by the hidden layer to perform nonlinear transformations and extract feature information. The output layer is connected

 doi:10.20944/preprints202405.1347.v1

to the hidden layers, and the final output is obtained through linear transformation by the fully connected layer. The hidden layers comprise two layers, with a hidden state dimension of 64.

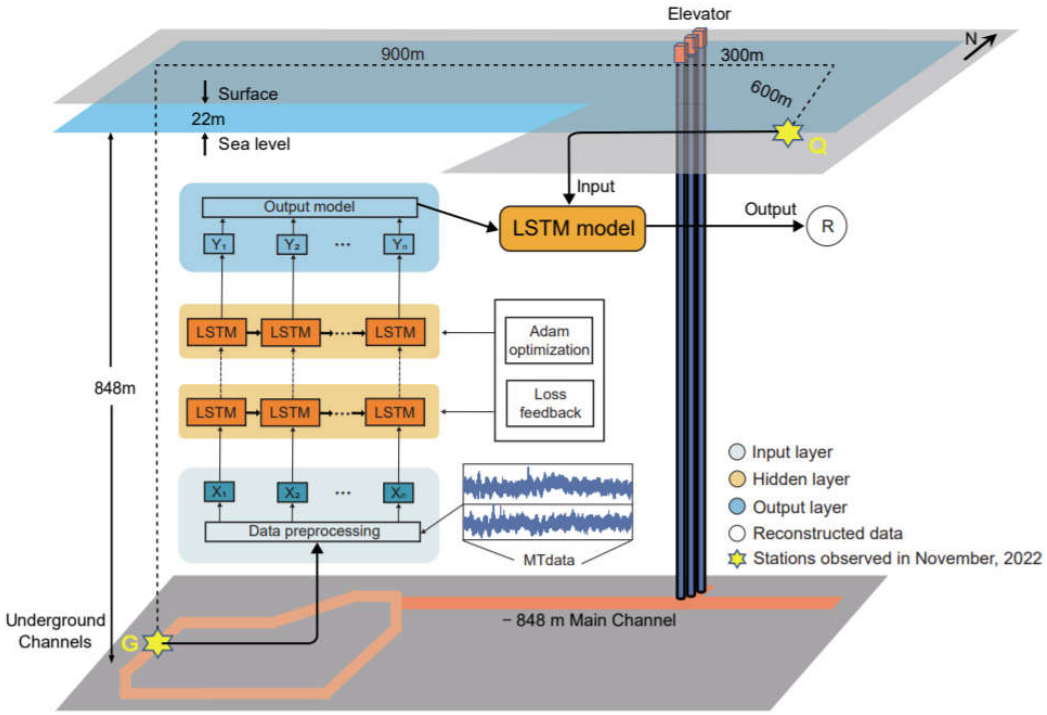

Figure 3. Flowchart of electromagnetic data reconstruction using LSTM neural network based on underground observations.

It is necessary to preprocess raw observation data through data normalization [62] to accelerate the gradient descent,

$$x = \frac{x_i - x_{min}}{x_{max} - x_{min}}, \tag{9}$$

where x_i denotes the input data, x_{max} and x_{min} represent the maximum and minimum values of the input data, and x denotes the normalized data.

The loss function and optimization are two crucial parameters for training an LSTM recurrent neural network. The loss function calculates the misfit between the labeled and predicted values to assess the model's accuracy. The optimization adjusts the model parameters to minimize the loss function [63]. We employed the Adam optimization algorithm which is a gradient-based stochastic objective function optimization algorithm combining the advantages of AdaGrad algorithm for sparse gradient processing and RMSprop for nonstationary target processing. The Adam algorithm is easy to implement, efficient, and requires minimal memory [64]. The Mean Square Error (MSE) loss function is defined as,

$$loss(x, y) = \frac{1}{N}\sum_{i=1}^{N} |x - y|^2, \tag{10}$$

where x represents the measured data, and y represents the output data. MSE is a commonly used loss function in regression problems due to its differentiability and computational efficiency. During neural network training, model parameters are updated based on the loss function. The backpropagation algorithm calculates the gradient of the loss function with respect to the model parameters, facilitating their adjustment to minimize the loss function and achieve optimal model performance.

 doi:10.20944/preprints202405.1347.v1

3. Synthetic Experiments

Four types of simulated noise, including charge and discharge triangle waves, Gaussian noise, square waves, and peak noise, were randomly superimposed onto the synthetic time series with a sampling rate of 1000 Hz and a length of 10 s. Figure 4 illustrates the reconstruction results from the time series contaminated with these different types of noise. The reconstructed data effectively suppress the four typical types of EM noise, exhibiting a high degree of agreement between the reconstructed and original clean data in terms of waveform and amplitude.

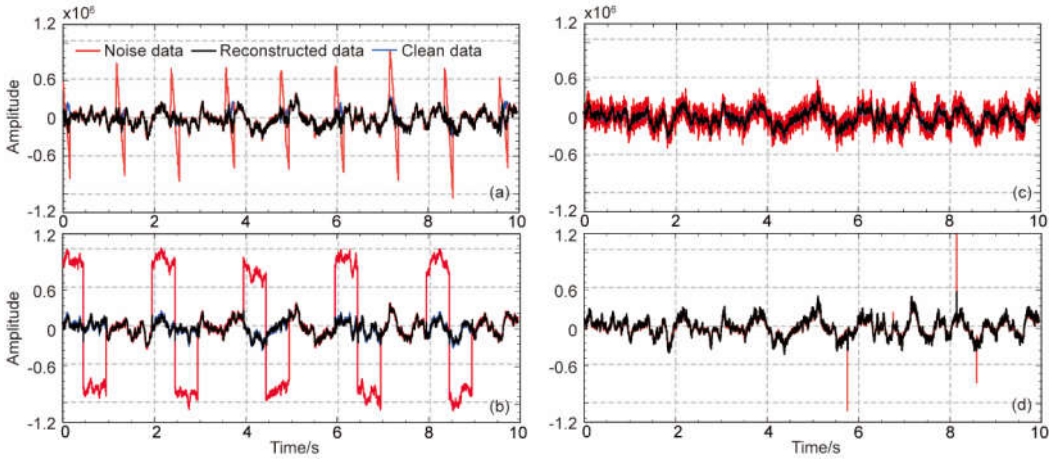

Figure 4. Data reconstruction from clean time series superimposed with different types of noise: (a) Charge and discharge triangle waves; (b) Square waves; (c) Gaussian noise; (d) Peak noise. Red lines represent the noisy data, blue lines represent the clean data, and black lines represent the reconstructed data.

To further assess the robustness of the reconstruction technique, the four types of noise were randomly combined and added to the original time series. Figure 5 illustrates the data reconstruction results for the timeseries contaminated with this complex noise combination. The reconstructed data shows a good agreement with the original clean data in terms of amplitude range, waveform shape, and developmental trend, even under the influence of complex random noise. Minor differences observed in the reconstructed data are considered acceptable, given the significant distortion characteristics associated with noise-containing data.

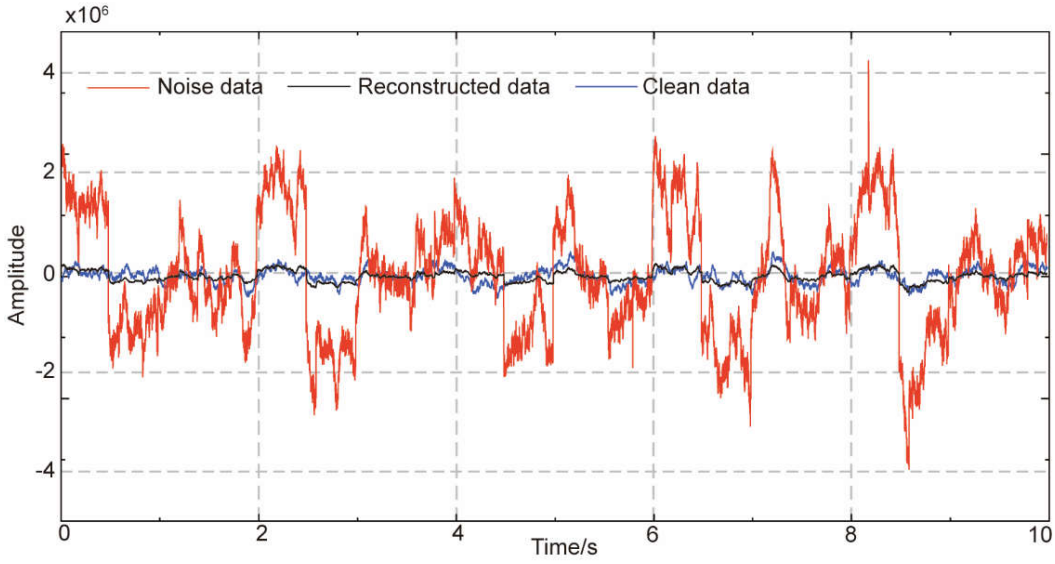

 doi:10.20944/preprints202405.1347.v1

Figure 5. Data reconstruction from timeseries superimposed with four types of noise. Red lines represent the noise data, blue lines represent the clean data, and black lines represent the reconstructed data.

The mean absolute percentage error (MAPE, Equation (11)) and the symmetric mean absolute percentage error (SMAPE, Equation (12)) were employed as evaluation metrics to assess the denoising effect,

$$MAPE = \frac{100\%}{n}\sum_{i=1}^{n}\left|\frac{\overline{y_i}-y_i}{y_i}\right|, \quad (11)$$

$$SMAPE = \frac{100\%}{n}\sum_{i=1}^{n}\frac{|\overline{y_i}-y_i|}{\frac{|\overline{y_i}|+|y_i|}{2}}, \quad (12)$$

where, n represents the number of samples, y denotes the original data, and $\overline{y}$ indicates the reconstructed data. MAPE measures the mean percentage error between the original and reconstructed data, while SMAPE incorporates the relative error into the assessment. Lower values of both MAPE and SMAPE indicate better denoising performance.

Quantitative evaluation results for the reconstructed data depicted in Figures 4 and 5 are summarized in Table 1. The findings indicate that for the four typical single noise datasets, the MAPE is approximately 2%, with the SMAPE less than 1%. Additionally, for the randomly combined noise datasets, the MAPE is only 3.85%, with an SMAPE of 1.09%. These results indicate that the LSTM network model effectively suppresses noise components, whether dealing with single-type noise data or complex multi-noise interference, highlighting the method's efficacy and reliability.

Table 1. Evaluation metrics for different noise suppression effects.

Noise	MAPE (%)	SMAPE (%)
Charge and discharge triangle wave	1.9222	0.6738
Square wave	1.7582	0.5977
Gaussian noise	2.0160	0.5724
Peak noise	1.6031	0.5099
Combined noise	3.8490	1.0905

4. Application to Observed Data Sets

4.1. Data

The EM observation data utilized for method validation were obtained from HNLab in China. HNLab was repurposed from a large closed coal mine and is situated over 100 km away from the TanLu fault zone in the east and approximately 200 km away from the junction of the South China Block and the North China Block in the south [16]. The underground environment at HNLab is characterized by an 870-meter-thick sedimentary cover, which effectively attenuates high-frequency anthropogenic EM noises. This attenuation facilitates high-quality, stable, and weak EM field observations underground. In contrast, ground-level observations are subject to complex and time-varying noise characteristics [19].

We utilized synchronous observations from underground point G (-848 meters at sea level) and ground point Q (+22 meters at sea level) (Figure 3) for model learning and signal reconstruction. Data were observed on November 5, 2022, at a sampling rate of 1000 Hz. Due to ongoing infrastructure renovations at HNLab, improvements in electrode deployments are still necessary, so only magnetic field data were used in this study. Both horizontal components, Hx (north-south) and Hy (east-west), were employed as multi-dimensional inputs for LSTM network model training. Subsequently, the noisy segments of the synchronous ground data were reconstructed using the trained LSTM network model. Larger datasets allow for the utilization of more hidden layers and neurons during neural network model training, reducing the likelihood of overfitting [65]. A sufficient large and high-

 doi:10.20944/preprints202405.1347.v1

quality dataset is essential for a robust training model. We used nighttime data for processing and analysis to avoid the impact of human-induced noise during daytime hours.

4.2. Processing and Results

A total of 10 minutes of normalized magnetic field data were partitioned into training, validation, and test datasets, accounting for 80%, 10%, and 10% of the data, respectively. We Employed a multivariate and multi-step sliding time window approach for model training. This method introduces a lag effect in trend perception, causing a phase shift in the reconstructed data. However, this phase shift can be easily corrected in the time domain by referencing the original data.

Figure 6 illustrates comparisons between the original and reconstructed ground Hx time series spanning one minute, sampled at 1000 Hz. Additionally, the synchronous underground data used in the model training are also shown. Previous study has indicated an approximate one to two orders of magnitude difference in the high-frequency band (> 1) Hz between the underground and ground magnetic field data [19]. Thanks to the attenuation effects of the conductive cover layer, underground data are not contaminated with significant noise disturbances present at the ground level. The ground data near the 27 and 50-second show obvious impulse noises that are absent in the underground data (Figure 6). The results exhibit good agreement in amplitudes between the reconstructed and observed ground data, with both sets showing roughly consistent waveforms. In addition, the noise in the observed data is significantly suppressed in the reconstructed signals, particularly regarding the impulse noise near 27 s and 50 seconds (Figure 6). Notably, the reconstructed data exhibit less high-frequency information compared to the observed data. Xie et al. [19] conducted a comparative analysis between original underground data and low-pass filtered ground data, indicating that the attenuation of the cover layer at HNLab can be approximately considered a low-pass filter with a cutoff frequency of 1 Hz. This finding explains the inconsistencies in local details between the original and reconstructed data (Figure 6). We conducted model training with underground data and performed data reconstruction with the original ground data. The difference between the two datasets in spectral components in the high-frequency band resulted in the absence of high-frequency information in the reconstructed ground signals.

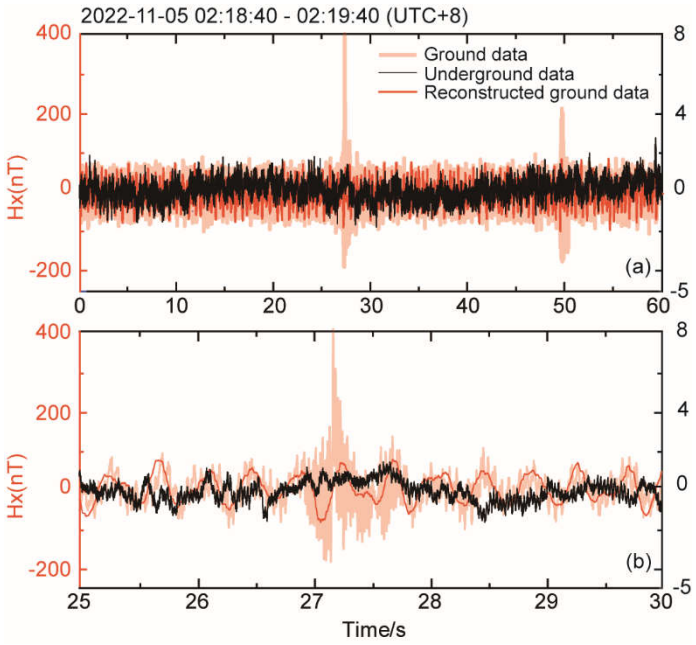

Figure 6. Reconstruction of ground Hx component using original data. (a) One-minute data; (b) Five-second data. Light orange lines represent the original ground data, orange lines represent the reconstructed data, and black lines represent the underground data.

 doi:10.20944/preprints202405.1347.v1

We further applied a 5th-order Chebyshev Type I low-pass filter to the ground data. Figure 7 illustrates the reconstruction of the ground Hx component using 100 Hz low-pass filtered data. Compared to the results using the original data (Figure 6), Figure 7 shows better agreement in amplitude and waveform between the filtered observation data and the corresponding reconstructions. The reconstructed data exhibit substantial suppression of high-frequency noise present in the observation data, notably at two specific instances (around 27 s and 50 s).

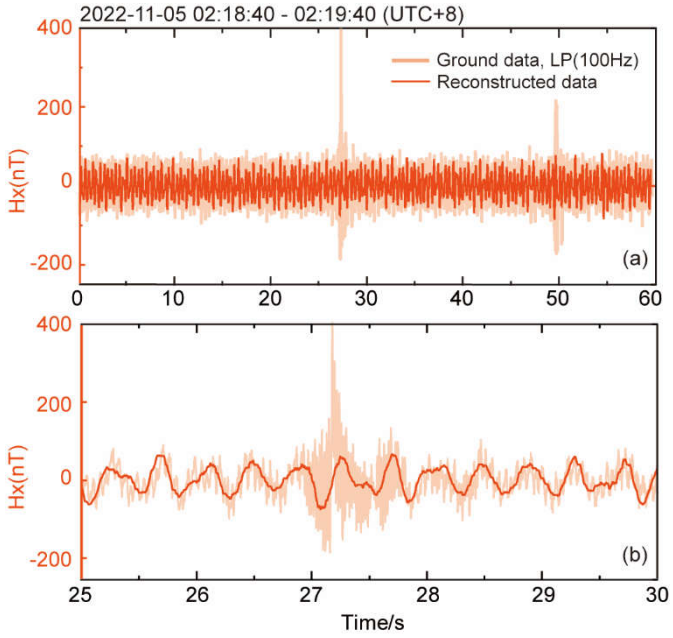

Figure 7. Reconstruction of ground Hx component using 100 Hz low-pass filtered data. (a) One-minute data; (b) Five-second data. Light orange lines represent the ground data, and orange lines represent the reconstructed data.

Xie et al. [19] suggest that the ground and underground data are roughly at the same level in the low-frequency band of < 1 Hz. Figure 8 depicts the reconstruction results using the 1 Hz low-pass filtered ground data. The results indicate good agreement in both amplitude and waveform between the filtered ground data and the corresponding reconstructed data. Additionally, the noise around 27 s is significantly suppressed in the reconstructed data.

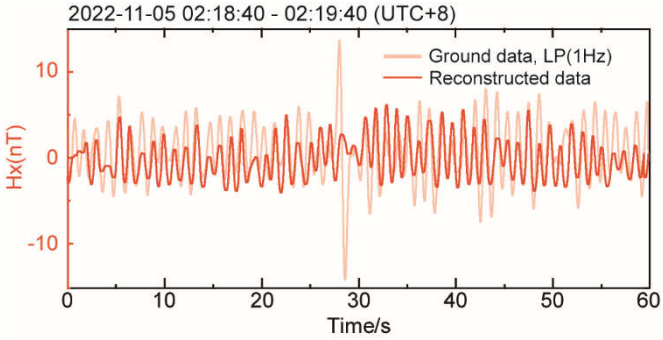

Figure 8. Reconstruction of ground Hx component using 1 Hz low-pass filtered data. Light orange lines represent the ground data, and orange lines represent the reconstructed data.

Figure 9 illustrates comparisons of the power spectral density (PSD) between the ground data and the corresponding reconstructed data. Both the original and low-pass filtered data were used in the processing. The data reconstruction based on the LSTM model, derived from the underground data, suggests a spectrum component absence or significant attenuation in the high frequency band

 doi:10.20944/preprints202405.1347.v1

of the reconstructed results. This is clearly indicated in the PSD of the original data, where the reconstructed signals exhibit lower amplitude than the observed data in the high-frequency band of > 10 Hz (Figure 9a). Similar results are suggested in Figure 9b, where both PSDs in the frequency band of > 100 Hz have a low amplitude less than -100 dB due to the 100 Hz low-pass filtering. For the 1 Hz filtered data, the coincident reconstructed and filtered data in the frequency band of > 10 Hz are lower than -100 dB, while the reconstructed data show slightly higher amplitude in the frequency band of 1 – 10 Hz. Although the conductive cover at HNLab is considered a low-pass filter with a cutoff frequency of 1 Hz, this natural low-pass filter is an approximation based on the definition of skin depth [19]. Therefore, in the stopband (> 1Hz), the reconstructed data show slightly higher amplitude compared to data filtered through a digital low-pass filter defined with a stronger attenuation coefficient. Focusing on the low-frequency band, all three cases of PSD indicate good agreement between the observed data and reconstructed data. These results suggest that the reconstructed ground data effectively retain the essential spectrum information in the low-frequency band.

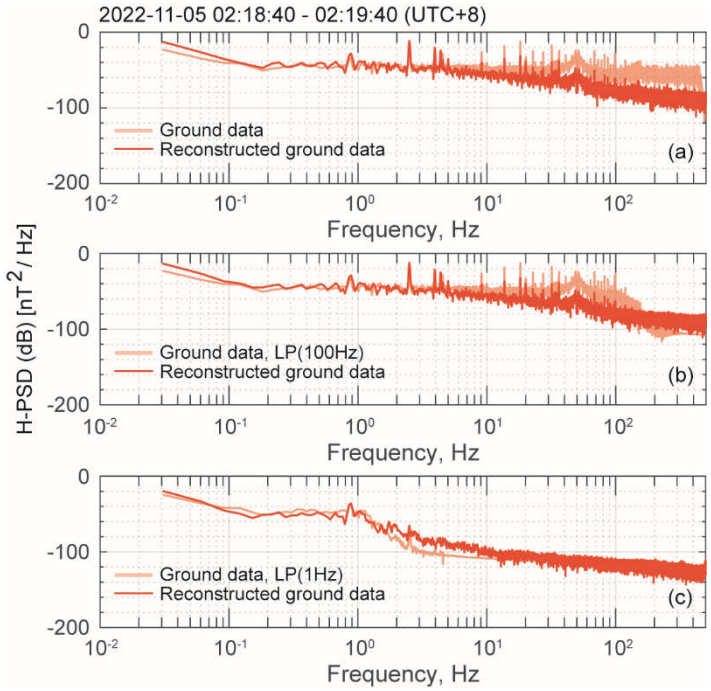

Figure 9. Power spectral density of ground and reconstructed data. The ground data used are the original data (a), the 100 Hz low-pass filtered data (b), and the 1 Hz low-pass filtered data (c).

The PSDs illustrate stacked results derived from different windows. We further calculated the power spectral probability density functions (PDFs) [66] to check variations in the power spectral density during the entire period. Figure 10 presents comparisons of the PDFs between the ground data and the corresponding reconstructed data. In the frequency band of < 100 Hz, the results derived from the original and 100 Hz low-pass filtered data are similar, with the reconstructed data > 10 Hz presenting lower PDF values (Figure 10a,b). In contrast, both the 1 Hz filtered data and the reconstructed data exhibit PDF amplitudes less than -50 dB in the stopband (> 1 Hz). In the lower frequency band, the PDFs of the reconstructed data are in agreement with the original and/or filtered ground data (Figure 10c). Additionally, the PDFs of the reconstructed data present more focused distributions in the low frequency band, indicating that random strong noise is effectively suppressed using the LSTM model. Both PSD and PDF results demonstrate that our signal reconstruction method is robust in noise suppression while preserving the effective components of the original data. However, a limitation of this approach is the absence of the high-frequency information in the reconstructed data caused by the LSTM model being trained with the attenuated underground data.

 doi:10.20944/preprints202405.1347.v1

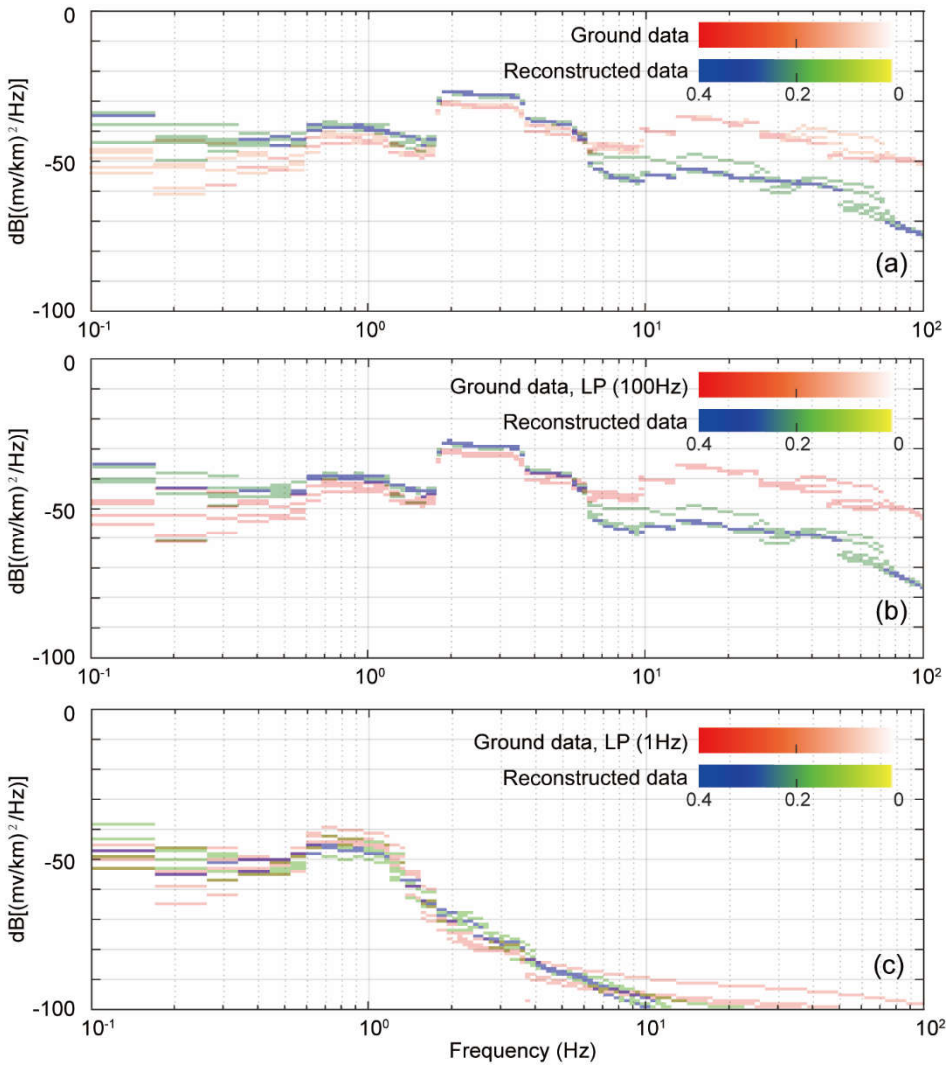

Figure 10. Probability density functions of ground and reconstructed data. The ground data used are the original data (a), the 100 Hz low-pass filtered data (b), and the 1 Hz low-pass filtered data (c).

Figure 11 illustrates the comparisons derived from one-dimensional continuous wavelet transform between the ground data and the corresponding reconstructed data using a Morse wavelet. Both the original and reconstructed data were employed for analysis. Notably, both the original and filtered data exhibit obvious interference noise around 2:19:10, which is significantly suppressed in the reconstructed data. Consistent with the results of PSD and PDFs (Figures 9 and 10), the wavelet spectra of the reconstructed signals align with the original and/or filtered data in a certain lower frequency band, demonstrating more stable and noise-free features in the reconstructed data. Furthermore, Figure 11 highlights that due to inherent differences in frequency components between the model training data (underground data) and the target processing data (ground data), there will be a certain loss of high-frequency components in the reconstructed ground data. This consideration is important for practical applications.

 doi:10.20944/preprints202405.1347.v1

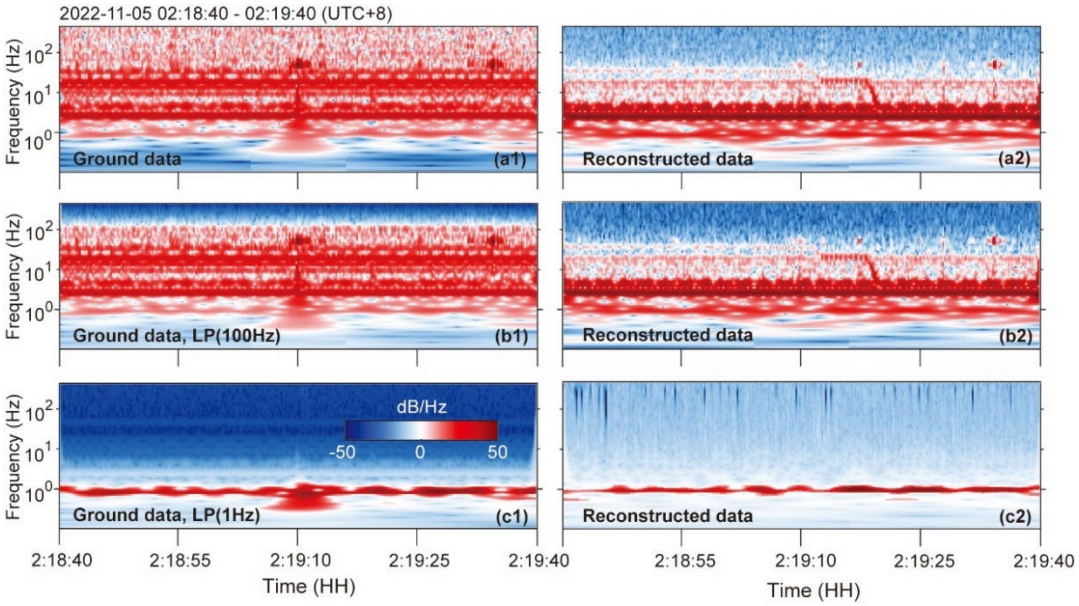

Figure 11. Results of the continuous wavelet transform of ground data (left panels) and corresponding reconstructed data (right panels). The ground data used are the original data (a), the 100 Hz low-pass filtered data (b), and the 1 Hz low-pass filtered data (c).

5. Discussion and Conclusions

This study presents an EM data reconstruction method utilizing LSTM recurrent neural networks, trained on data observed in deep underground environments known for their low-background noise advantages. The LSTM network model is specifically tailored to capture the complex coupling relationships and dynamic characteristics inherent in multi-channel EM field components. The method focuses on reconstructing strong noise segments synchronously observed at noisy stations, particularly typical ground stations. Key characteristics of this approach include:

(1) Typical MT noise suppression methods utilizing CNNs or RNNs are primarily supervised learning algorithms. The effectiveness and robustness of both model training and denoising processing hinge on the availability of diverse and extensive training datasets encompassing both signals and noises. Training datasets often include synthetic data representing typical types of noise and/or high-quality measured signals, aiding in noise identification, separation, and reconstruction for specific observed signals [41–43]. However, EM field signals exhibit strong spatial and weak temporal correlation and are susceptible to contamination from random and complex noise sources. As a result, synthetic data-derived signal and noise patterns may not fully encapsulate the diverse characteristics of observed data, limiting the applicability and reliability of these methods. The inherent complexities and variability of real-world EM field data necessitate novel approaches that can adapt and generalize effectively to diverse noise conditions and signal characteristics.

In this study, both the training dataset and the processing dataset are synchronously observed, indicating strong inherit correlations and coupling between the two datasets within a specific spatial range, particularly with respect to magnetic field components. Unlike approaches that focused solely on characterizing the morphological contours of noise, our method leverages the robust spatial correlation of EM fields and the high-quality underground data. This approach utilizes the intrinsic characteristics of synchronous observations and the coupling between different EM components obtained through deep learning to achieve data reconstruction. The method capitalizes on the strong spatial correlation within the EM field signals and the high signal-to-noise ratio characteristics of underground data. Importantly, this process does not require prior knowledge of noise types, and it reduces the necessary sample size for the training dataset compared to traditional methods, thereby offering advantages in processing efficiency. Moreover, traditional methods typically involve independent training and processing for specific single components. In contrast, our multidimensional model reconstruction approach not only comprehensively learns the

 doi:10.20944/preprints202405.1347.v1

spatiotemporal characteristics of individual components but also establishes a robust network mapping based on the couplings among different EM components. This holistic approach enables more effective and efficient data reconstruction while capturing complex interdependencies among various EM field parameters.

(2) The methodology employed in this study shares formal similarities with the remote reference method, as both approaches utilizes reference station data observed in low EM noise environments and leverage the strong spatial correlation exhibited by EM fields in regional areas. However, there are fundamental distinctions between them: Firstly, traditional remote reference methods like those proposed by Gamble et al. [27] and Clarke et al. [28] , along with variants such as the remote reference with 'magnetic control' (RRMT) introduced by Varentsov [67] and Varentsov [68], operate in the frequency domain. These methods capitalize on the lack of noise correction between remote and local channels to suppress noise levels in the power spectral density matrix. In contrast, the method presented in this study utilizes deep learning technology to establish a network mapping for time series reconstruction of noise-affected data segments in the time domain. Secondly, traditional remote reference methods focus on signal correlation between local and remote stations, calculating correlations independently for each component. In contrast, our method considers correlations among all channels from both local and remote stations. Varentsov [67] introduces the horizontal magnetic tensor into the traditional remote reference method, which also incorporates constraints arising from the correlation between different magnetic field components.

(3) In recent years, deep learning has found widespread application in the analysis of seismic data [69,70], gravity data [71], and various other geophysical field observations. These applications have demonstrated highly effective processing and denoising capabilities for time series data. The LSTM network model training and signal reconstruction method proposed in this study, which is based on underground EM observation data, can be extended to encompass other deep underground observation experiments involving multiple geophysical fields. This extension would entail adapting the model training and processing for individual geophysical fields or multiple coupled geophysical fields, thereby serving as a preprocessing tool to capture weak signals and address scientific challenges. It's important to recognize that time series data from different geophysical field observations exhibit diverse patterns and are subject to varying types of noise. Consequently, adjustments to model parameters will be necessary when applying this method to process other multi-geophysical field data. Each field may require tailored approaches to optimize performance and achieve accurate signal reconstruction and denoising effects.

(4) The complex noise in the reconstructed data is effectively suppressed with the LSTM network model, benefiting from the attenuation to high-frequency interference noise when penetrating through the conductive cover layer. However, this attenuation also leads to differences in frequency components between the training data and the target reconstructed data, resulting in an amplitude loss of high-frequency information in the reconstructed signal. Therefore, when targeting high-frequency information in processing, the method is no longer directly applicable, and further amplitude correction of the effective signal becomes necessary.

Author Contributions: Conceptualization, Y.T. and C.X.; writing—original draft preparation, Y.T. and C.X.; writing—review and editing, Y.T., C.X. and Y.W. All authors have read and agreed to the published version of the manuscript.

Funding: This research was funded by the National Natural Science Foundation of China, grant number 42074083, 62127815, 42150201, U1839208 and the National Key Research and Development Program of China, grant number 2023YFF0803301.

Institutional Review Board Statement: Not applicable.

Informed Consent Statement: Not applicable.

Data Availability Statement: The datasets generated during and/or analysed during the current study are available from the corresponding author on reasonable request.

Acknowledgments: This work was supported by the High-performance Computing Platform of China University of Geosciences Beijing.

 doi:10.20944/preprints202405.1347.v1

Conflicts of Interest: The authors declare no conflicts of interest.

References

1. Kang, K.J.; Cheng, J.P.; Chen, Y.H.; Li, Y.J.; Shen, M.B.; Wu, S.Y.; Yue, Q. Status and Prospects of a Deep Underground Laboratory in China. J. Phys.: Conf. Ser. 2010, 203, 012028, doi:10.1088/1742-6596/203/1/012028.
2. Smith, N.J.T. The SNOLAB Deep Underground Facility. Eur. Phys. J. Plus 2012, 127, 108, doi:10.1140/epjp/i2012-12108-9.
3. Mizukoshi, K.; Taishaku, R.; Hosokawa, K.; Kobayashi, K.; Miuchi, K.; Naka, T.; Takeda, A.; Tanaka, M.; Wada, Y.; Yorita, K. Measurement of Ambient Neutrons in an Underground Laboratory at Kamioka Observatory and Future Plan. In Proceedings of the Journal of Physics: Conference Series; IOP Publishing, 2020; Vol. 1468, p. 012247.
4. Palušová, V.; Breier, R.; Chauveau, E.; Piquemal, F.; Povinec, P.P. Natural Radionuclides as Background Sources in the Modane Underground Laboratory. Journal of environmental radioactivity 2020, 216, 106185, doi:10.1016/j.jenvrad.2020.106185.
5. Waysand, G.; Bloyet, D.; Bongiraud, J.P.; Collar, J.I.; Dolabdjian, C.; Le Thiec, P. First Characterization of the Ultra-Shielded Chamber in the Low-Noise Underground Laboratory (LSBB) of Rustrel-Pays d'Apt. Nuclear Instruments and Methods in Physics Research Section A: Accelerators, Spectrometers, Detectors and Associated Equipment 2000, 444, 336–339, doi:10.1016/S0168-9002(99)01377-7.
6. Daniels, K.A.; Harrington, J.F.; Wiseall, A.C.; Shoemark-Banks, E.; Hough, E.; Wallis, H.C.; Paling, S.M. Battery Earth: Using the Subsurface at Boulby Underground Laboratory to Investigate Energy Storage Technologies. Frontiers in Physics 2023, 11, 1249458, doi:10.3389/fphy.2023.1249458.
7. Pomansky, A.A. Underground Low Background Laboratories of the Baksan Neutrino Observatory. Nuclear Instruments and Methods in Physics Research Section B: Beam Interactions with Materials and Atoms 1986, 17, 406–410, doi:10.1016/0168-583X(86)90173-4.
8. Naticchioni, L.; Iudochkin, N.; Yushkin, V.; Majorana, E.; Perciballi, M.; Ricci, F.; Rudenko, V. Seismic Noise Background in the Baksan Neutrino Observatory. Eur. Phys. J. Plus 2022, 137, 124, doi:10.1140/epjp/s13360-021-02317-8.
9. Naticchioni, L.; Perciballi, M.; Ricci, F.; Coccia, E.; Malvezzi, V.; Acernese, F.; Barone, F.; Giordano, G.; Romano, R.; Punturo, M. Microseismic Studies of an Underground Site for a New Interferometric Gravitational Wave Detector. Classical and Quantum Gravity 2014, 31, 105016, doi:10.1088/0264-9381/31/10/105016.
10. Naticchioni, L.; Boschi, V.; Calloni, E.; Capello, M.; Cardini, A.; Carpinelli, M.; Cuccuru, S.; D'Ambrosio, M.; De Rosa, R.; Di Giovanni, M. Characterization of the Sos Enattos Site for the Einstein Telescope. In Proceedings of the Journal of Physics: Conference Series; IOP Publishing, 2020; Vol. 1468, p. 012242.
11. Gaffet, S.; Guglielmi, Y.; Virieux, J.; Waysand, G.; Chwala, A.; Stolz, R.; Emblanch, C.; Auguste, M.; Boyer, D.; Cavaillou, A. Simultaneous Seismic and Magnetic Measurements in the Low-Noise Underground Laboratory (LSBB) of Rustrel, France, during the 2001 January 26 Indian Earthquake. Geophysical Journal International 2003, 155, 981–990, doi:10.1111/j.1365-246X.2003.02095.x.
12. Waysand, G.; Barroy, P.; Blancon, R.; Gaffet, S.; Guilpin, C.; Marfaing, J.; Di Borgo, E.P.; Pyée, M.; Auguste, M.; Boyer, D. Seismo-Ionosphere Detection by Underground SQUID in Low-Noise Environment in LSBB-Rustrel, France. The European Physical Journal-Applied Physics 2009, 47, 12705, doi:10.1051/epjap:2008186.
13. Sun, H.; CHEN, X.; WEI, Z.; ZHANG, M.; ZHANG, G.; NI, S.; CHU, R.; XU, J.; CUI, X.; XING, L. A Preliminary Study on the Ultra-Wide Band Ambient Noise of the Deep Underground Based on Observations of the Seismometer and Gravimeter. Chinese Journal of Geophysics 2022, 65, 4543–4554.
14. Wang, Z.; WANG, Y.; XU, R.; LIU, T.; FU, G.; SUN, H. Environmental Noise Assessment of Underground Gravity Observation in Huainan and the Potential Capability of Detecting Slow Earthquake. Chinese Journal of Geophysics 2022, 65, 4555–4568.
15. Wang, Y.; JIAN, Y.; HE, Y.; MIAO, Q.; TENG, J.; WANG, Z.; RONG, L.; QIU, L.; XIE, C.; ZHANG, Q. Underground Laboratories and Deep Underground Geophysical Observations. Chinese Journal of Geophysics 2022, 65, 4527–4542.
16. Wang, Y.; Yang, Y.; Sun, H.; Xie, C.; Zhang, Q.; Cui, X.; Chen, C.; He, Y.; Miao, Q.; Mu, C.; et al. Observation and Research of Deep Underground Multi-Physical Fields—Huainan −848 m Deep Experiment. Sci. China Earth Sci. 2023, 66, 54–70, doi:10.1007/s11430-022-9998-2.
17. Guo, L.; WANG, B.; SONG, X.; WANG, Y.; JIN, C.; YAO, S.; SHI, Y. Continuous Observation of Geomagnetic Total-Field at the Underground Laboratory in Huainan City, China and Its Time-Varying Characteristics. Chinese Journal of Geophysics 2024, 67, 820–828.
18. Wan, W.; CHEN, C.; WANG, Y.; MU, C.; HE, Y.; WANG, C. Comparative Analysis of Surface and Deep Underground Seismic Ambient Noise. Chinese Journal of Geophysics 2024, 67, 793–808.

19. Xie, C.; Chen, C.; Liu, C.; Wan, W.; Jin, S.; Ye, G.; Jing, J.; Wang, Y. Insights from Underground Laboratory Observations: Attenuation-Induced Suppression of Electromagnetic Noise. The European Physical Journal Plus 2024, 139, 218, doi:10.1140/epjp/s13360-024-05033-1.
20. Wang, H.; Campanyà, J.; Cheng, J.; Zhu, G.; Wei, W.; Jin, S.; Ye, G. Synthesis of Natural Electric and Magnetic Time-series Using Inter-station Transfer Functions and Time-series from a Neighboring Site (STIN): Applications for Processing MT Data. JGR Solid Earth 2017, 122, 5835–5851, doi:10.1002/2017JB014190.
21. Zhao, G.; Zhang, X.; Cai, J.; Zhan, Y.; Ma, Q.; Tang, J.; Du, X.; Han, B.; Wang, L.; Chen, X.; et al. A Review of Seismo-Electromagnetic Research in China. Sci. China Earth Sci. 2022, 65, 1229–1246, doi:10.1007/s11430-021-9930-5.
22. Egbert, G.D.; Booker, J.R. Robust Estimation of Geomagnetic Transfer Functions. Geophysical Journal of the Royal Astronomical Society 1986, 87, 173–194, doi:10.1111/j.1365-246X.1986.tb04552.x.
23. Chave, A.D.; Thomson, D.J. Some Comments on Magnetotelluric Response Function Estimation. Journal of Geophysical Research: Solid Earth 1989, 94, 14215–14225, doi:10.1029/JB094iB10p14215.
24. Jones, A.G.; Chave, A.D.; Egbert, G.; Auld, D.; Bahr, K. A Comparison of Techniques for Magnetotelluric Response Function Estimation. Journal of Geophysical Research: Solid Earth 1989, 94, 14201–14213, doi:10.1029/JB094iB10p14201.
25. Mebane Jr., J.S.S., W.R. Robust Estimation and Outlier Detection for Overdispersed Multinomial Models of Count Data. American Journal of Political Science 2004, 48, 392–411, doi:10.1111/j.0092-5853.2004.00077.x.
26. Goubau, W.M.; Gamble, T.D.; Clarke, J. Magnetotelluric Data Analysis: Removal of Bias. GEOPHYSICS 1978, 43, 1157–1166, doi:10.1190/1.1440885.
27. Gamble, T.D.; Goubau, W.M.; Clarke, J. Magnetotellurics with a Remote Magnetic Reference. GEOPHYSICS 1979, 44, 53–68, doi:10.1190/1.1440923.
28. Clarke, J.; Gamble, T.D.; Goubau, W.M.; Koch, R.H.; Miracky, R.F. Remote-Reference Magnetotellurics: Equipment and Procedures. Geophysical Prospecting 1983, 31, 149–170, doi:10.1111/j.1365-2478.1983.tb01047.x.
29. Egbert, G.D. Robust Multiple-Station Magnetotelluric Data Processing. Geophysical Journal International 1997, 130, 475–496, doi:10.1111/j.1365-246X.1997.tb05663.x.
30. Egbert, G. Processing And Interpretation Of Electromagnetic Induction Array Data. Surveys in Geophysics 2002, 23, 207–249, doi:10.1023/A:1015012821040.
31. Smirnov, M.Y.; Egbert, G.D. Robust Principal Component Analysis of Electromagnetic Arrays with Missing Data. Geophysical Journal International 2012, 190, 1423–1438, doi:10.1111/j.1365-246X.2012.05569.x.
32. Zhou, C.; Tang, J.; Yuan, Y. Multi-Reference Array MT Data Processing Method. Oil Geophysical Prospecting 2020, 55(6), 1373–1382, doi:DOI: 10.13810/j.cnki.issn.1000-7210.2020.06.023 .
33. Garcia, X.; Jones, A.G. Robust Processing of Magnetotelluric Data in the AMT Dead Band Using the Continuous Wavelet Transform. GEOPHYSICS 2008, 73, 223–234, doi:10.1190/1.2987375.
34. Cai, J.-H.; Tang, J.-T.; Hua, X.-R.; Gong, Y.-R. An Analysis Method for Magnetotelluric Data Based on the Hilbert–Huang Transform. Exploration Geophysics 2009, 40, 197–205, doi:10.1071/EG08124.
35. Chen, J.; Heincke, B.; Jegen, M.; Moorkamp, M. Using Empirical Mode Decomposition to Process Marine Magnetotelluric Data. Geophysical Journal International 2012, 190, 293–309, doi:10.1111/j.1365-246X.2012.05470.x.
36. Tang, J.T.; Li, G.; Xiao, X. Strong Noise Separation for Magnetotelluric Data Based on a Signal Reconstruction Algorithm of Compressive Sensing. Chinese J. Geophys. (in Chinese) 2017, 60(9), 3642–3654, doi:doi: 10.6038/cjg20170928.
37. Kappler, K.N. A Data Variance Technique for Automated Despiking of Magnetotelluric Data with a Remote Reference. Geophysical Prospecting 2012, 60, 179–191, doi:10.1111/j.1365-2478.2011.00965.x.
38. Ogawa, H.; Asamori, K.; Negi, T.; Ueda, T. A Novel Method for Processing Noisy Magnetotelluric Data Based on Independence of Signal Sources and Continuity of Response Functions. Journal of Applied Geophysics 2023, 213, 105012, doi:10.1016/j.jappgeo.2023.105012.
39. Dramsch, J. 70 Years of Machine Learning in Geoscience in Review. In Machine Learning in Geosciences; edited, Ed.; 2020; pp. 1–55.
40. Manoj, C.; Nagarajan, N. The Application of Artificial Neural Networks to Magnetotelluric Time-Series Analysis. Geophysical Journal International 2003, 153, 409–423, doi:10.1046/j.1365-246X.2003.01902.x.
41. Li, J.; Liu, Y.; Tang, J.; Ma, F. Magnetotelluric Noise Suppression via Convolutional Neural Network. GEOPHYSICS 2023, 88, WA361–WA375, doi:10.1190/geo2022-0258.1.
42. Li, J.; Liu, Y.; Tang, J.; Peng, Y.; Zhang, X.; Li, Y. Magnetotelluric Data Denoising Method Combining Two Deep-Learning-Based Models. GEOPHYSICS 2023, 88, E13–E28.
43. Han, Y.; An, Z.; Di, Q.; Wang, Z.; Kang, L. Research on Noise Suppression of Magnetotelluric Signal Based on Recurrent Neural Network. Chinese Journal of Geophysics 2023, 66, 4317–4331.

44. Zhang, L.; Li, G.; Chen, H.; Tang, J.; Yang, G.; Yu, M.; Hu, Y.; Xu, J.; Sun, J. Identification and Suppression of Multicomponent Noise in Audio Magnetotelluric Data Based on Convolutional Block Attention Module. IEEE Transactions on Geoscience and Remote Sensing 2024, 62, 1–15.
45. Feng, C.; Li, Y.; Wu, Y.; Duan, S. A Noise Suppression Method of Marine Magnetotelluric Data Using K-SVD Dictionary Learning. Chinese Journal of Geophysics 2022, 65, 1853–1865.
46. Li, J.; Peng, Y.; Tang, J.; Li, Y. Denoising of Magnetotelluric Data Using K-SVD Dictionary Training. Geophysical Prospecting 2021, 69, 448–473, doi:10.1111/1365-2478.13058.
47. Li, G.; Gu, X.; Ren, Z.; Wu, Q.; Liu, X.; Zhang, L.; Xiao, D.; Zhou, C. Deep Learning Optimized Dictionary Learning and Its Application in Eliminating Strong Magnetotelluric Noise. Minerals 2022, 12, doi:10.3390/min12081012.
48. Li, G.; Liu, X.; Tang, J.; Deng, J.; Hu, S.; Zhou, C.; Chen, C.; Tang, W. Improved Shift-Invariant Sparse Coding for Noise Attenuation of Magnetotelluric Data, Earth. Planets and Space 2020, 72, 45.
49. Liu, X.; Li, G.; Li, J.; Zhou, X.; Gu, X.; Zhou, C.; Gong, M. Self-Organizing Competitive Neural Network Based Adaptive Sparse Representation for Magnetotelluric Data Denoising. Journal of Physics: Conference Series 2023, 2651, 012129, doi:10.1088/1742-6596/2651/1/012129.
50. Cunningham, P.; Cord, M.; Delany, S.J. Supervised Learning. In Machine Learning Techniques for Multimedia; Cord, M., Cunningham, P., Eds.; Cognitive Technologies; Springer Berlin Heidelberg: Berlin, Heidelberg, 2008; pp. 21–49 ISBN 978-3-540-75170-0.
51. Schuster, M.; Paliwal, K.K. Bidirectional Recurrent Neural Networks. IEEE Trans. Signal Process. 1997, 45, 2673–2681, doi:10.1109/78.650093.
52. LeCun, Y.; Bengio, Y.; Hinton, G. Deep Learning. Nature 2015, 521, 436–444, doi:10.1038/nature14539.
53. Salehinejad, H.; Sankar, S.; Barfett, J.; Colak, E.; Valaee, S. Recent Advances in Recurrent Neural Networks 2018.
54. Graves, A. Supervised Sequence Labelling with Recurrent Neural Networks; Studies in Computational Intelligence; Springer Berlin Heidelberg: Berlin, Heidelberg, 2012; Vol. 385; ISBN 978-3-642-24796-5.
55. Van Houdt, G.; Mosquera, C.; Nápoles, G. A Review on the Long Short-Term Memory Model. Artif Intell Rev 2020, 53, 5929–5955, doi:10.1007/s10462-020-09838-1.
56. Hochreiter, S.; Schmidhuber, J. Long Short-Term Memory. Neural Computation 1997, 9, 1735–1780, doi:10.1162/neco.1997.9.8.1735.
57. Malhotra, P.; Vig, L.; Shroff, G.; Agarwal, P. Long Short Term Memory Networks for Anomaly Detection in Time Series. Computational Intelligence 2015.
58. Wan, S.; Qi, L.; Xu, X.; Tong, C.; Gu, Z. Deep Learning Models for Real-Time Human Activity Recognition with Smartphones. Mobile Netw Appl 2020, 25, 743–755, doi:10.1007/s11036-019-01445-x.
59. Yang, J.; Yao, S.; Wang, J. Deep Fusion Feature Learning Network for MI-EEG Classification. Ieee Access 2018, 6, 79050–79059, doi:10.1109/ACCESS.2018.2877452.
60. Staudemeyer, R.C.; Morris, E.R. Understanding LSTM -- a Tutorial into Long Short-Term Memory Recurrent Neural Networks 2019.
61. Van Houdt, G.; Mosquera, C.; Nápoles, G. A Review on the Long Short-Term Memory Model. Artif Intell Rev 2020, 53, 5929–5955, doi:10.1007/s10462-020-09838-1.
62. Huang, L.; Qin, J.; Zhou, Y.; Zhu, F.; Liu, L.; Shao, L. Normalization Techniques in Training Dnns: Methodology, Analysis and Application. IEEE transactions on pattern analysis and machine intelligence 2023, 45, 10173–10196, doi:10.1109/TPAMI.2023.3250241.
63. Chen, W.; Yang, L.; Zha, B.; Zhang, M.; Chen, Y. Deep Learning Reservoir Porosity Prediction Based on Multilayer Long Short-Term Memory Network. Geophysics 2020, 85, WA213–WA225, doi:10.1190/geo2019-0261.1.
64. Kingma, D.P.; Ba, J. Adam: A Method for Stochastic Optimization 2017.
65. Bouktif, S.; Fiaz, A.; Ouni, A.; Serhani, M.A. Optimal Deep Learning Lstm Model for Electric Load Forecasting Using Feature Selection and Genetic Algorithm: Comparison with Machine Learning Approaches. Energies 2018, 11, 1636, doi:10.3390/en11071636.
66. McNamara, D.E.; Buland, R.P. Ambient Noise Levels in the Continental United States. Bulletin of the seismological society of America 2004, 94, 1517–1527.
67. Varentsov, I. RRMC TECHNIQUE FIGHTS HIGHLY COHERENT EM NOISE, in Protokoll Uber Das 21 Kolloquium “EM Tiefenforschung.” In RRMC TECHNIQUE FIGHTS HIGHLY COHERENT EM NOISE, in Protokoll uber das 21 Kolloquium “EM Tiefenforschung”; edited., Ed.; 2005.
68. Varentsov, I.; Sokolova, E.; Martanus, E.; Nalivaiko, K.; Group System of Electromagnetic Field Transfer Operators for the BEAR Array of Simultaneous Soundings: Methods and Results. Izvestiya Physics of the Solid Earth 2003, 39, 118–148.
69. Dong, X.T.; Li, Y.; Yang, B.J. Desert Low-Frequency Noise Suppression by Using Adaptive DnCNNs Based on the Determination of High-Order Statistic. Geophysical Journal International 2019, 219, 1281–1299, doi:10.1093/gji/ggz363.

 doi:10.20944/preprints202405.1347.v1

70. Zhao, Y.; Li, Y.; Dong, X.; Yang, B. Low-Frequency Noise Suppression Method Based on Improved DnCNN in Desert Seismic Data. IEEE Geoscience and Remote Sensing Letters 2019, 16, 811–815, doi:10.1109/LGRS.2018.2882058.
71. Maiti, S.; Chiluvuru, R.K. A Deep CNN-LSTM Model for Predicting Interface Depth from Gravity Data over Thrust and Fold Belts of North East India. Journal of Asian Earth Sciences 2024, 259, 105881, doi:10.1016/j.jseaes.2023.105881.
72. Zhou, Y.; Chang, Y.; Chen, H.; Zhou, Y.; Ma, Y.; XIE, C.; He, Z.; Katsumi, H.; Han, P. Application of Reference-Based Blind Source Separation Method in the Reduction of near-Field Noise of Geomagnetic Measurements. CHINESE JOURNAL OF GEOPHYSICS-CHINESE EDITION 2019, 62, 572–586.